



Cite as
Nano-Micro Lett.
(2020) 12:111

Received: 23 February 2020
Accepted: 17 April 2020
© The Author(s) 2020

Surface-Modified Graphene Oxide/Lead Sulfide Hybrid Film-Forming Ink for High-Efficiency Bulk Nano-Heterojunction Colloidal Quantum Dot Solar Cells

Yaohong Zhang¹, Guohua Wu² ✉, Chao Ding¹, Feng Liu¹, Dong Liu¹, Taizo Masuda³, Kenji Yoshino⁴, Shuzi Hayase¹, Ruixiang Wang⁵ ✉, Qing Shen¹ ✉

✉ Guohua Wu, ghwu@snnu.edu.cn; Ruixiang Wang, wangruixiang@bucea.edu.cn; Qing Shen, shen@pc.uec.ac.jp

¹ Faculty of Informatics and Engineering, The University of Electro-Communications, Tokyo 182-8585, Japan

² School of Materials Science and Engineering, Shaanxi Normal University, Xi'an 710119, People's Republic of China

³ X-Frontier Division, Toyota Motor Corporation, Shizuoka 471-8571, Japan

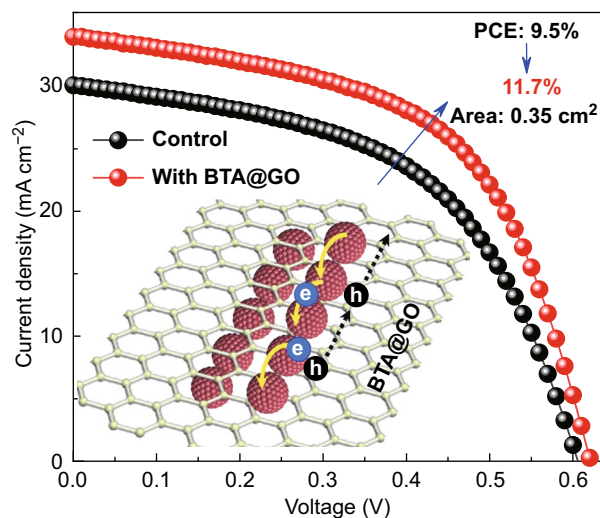
⁴ Department of Electrical and Electronic Engineering, University of Miyazaki, Miyazaki 889-2192, Japan

⁵ Beijing Engineering Research Centre of Sustainable Energy and Buildings, Beijing University of Civil, Engineering and Architecture, Beijing 102616, People's Republic of China

HIGHLIGHTS

- Butylamine-modified graphene oxide (BTA@GO) is first utilized in PbS colloidal quantum dots (CQDs) ink to deposit the active layer of colloidal quantum dot solar cells (CQDSCs).
- The BTA@GO improves the carrier transfer rate in the CQDs active layer and 11.7% conversion efficiency is achieved.

ABSTRACT Solution-processed colloidal quantum dot solar cells (CQDSCs) is a promising candidate for new generation solar cells. To obtain stable and high performance lead sulfide (PbS)-based CQDSCs, high carrier mobility and low non-radiative recombination center density in the PbS CQDs active layer are required. In order to effectively improve the carrier mobility in PbS CQDs layer of CQDSCs, butylamine (BTA)-modified graphene oxide (BTA@GO) is first utilized in PbS-PbX₂ (X=I⁻, Br⁻) CQDs ink to deposit the active layer of CQDSCs through one-step spin-coating method. Such surface treatment of GO dramatically upholds the intrinsic superior hole transfer peculiarity of GO and attenuates the hydrophilicity of GO in order to allow for its good dispersibility in ink solvent. The introduction of BTA@GO in CQDs layer can build up a bulk nano-heterojunction architecture, which provides a smooth charge carrier transport channel in turn improves the carrier mobility and conductivity, extends the carriers lifetime and reduces the trap density of PbS-PbX₂ CQDs film. Finally, the BTA@GO/PbS-PbX₂ hybrid CQDs film-based relatively large-area (0.35 cm²) CQDSCs shows a champion power conversion efficiency of 11.7% which is increased by 23.1% compared with the control device.



KEYWORDS Quantum dot solar cells; PbS colloidal quantum dots; Hole extraction; Graphene oxide; Surface modified

1 Introduction

Semiconductor colloidal quantum dots (CQDs) are attracting enormous attention in the next-generation photovoltaic applications due to their size-dependent bandgap tunability, facile solution-processed manufacturability and especially multiple exciton generation (MEG) effect [1, 2]. The photovoltaic performance of colloidal quantum dot solar cells (CQDSCs) has been significantly improved in the past few years by CQDs surface ligand modification [3–9], device architecture optimization [10–15], active layer deposition engineering [16–18], etc. Nevertheless, the performance of CQDSCs is still much lower than its theoretical efficiency (44.4%) [19, 20]. Recently, a certified record power conversion efficiency (PCE) of 16.6% has been achieved by $\text{Cs}_{0.5}\text{FA}_{0.5}\text{PbI}_3$ perovskite-based CQDSCs [19], and the PCE of lead sulfide (PbS)-based CQDSCs reached 13.3% with aperture area of 0.049 cm^2 [21]. There are many challenges and issues waiting to be solved on the way forward to further improve the performance of CQDSCs.

Photoexcited carrier diffusion length and recombination centers are crucial for CQDs active layer because they closely relate to the charge separation and collection efficiencies and short-circuit photocurrent density (J_{SC}) as well as open-circuit photovoltage (V_{OC}) of CQDSCs devices. The PCE of CQDSCs is also limited by the common trade-off between light absorption and charge carrier extraction in CQDs layer. To further balance the charge extraction efficiencies and light absorption, n-type semiconductor (i.e., ZnO) nanowire electrode with large electron diffusion coefficient has been introduced into CQDSCs to build a bulk heterojunction architecture in favor of improving the charge separation at the electrode/CQDs interface and electron diffusion length, which results in possible increase of the thickness of CQDs active layer [18, 22–25]. Although the use of nanowire electrode can improve the J_{SC} of the device to a certain extent due to the increased thickness of CQDs active layer, the V_{OC} and fill factor (FF) of these devices are usually deteriorated compared to the planar heterojunction CQDSCs. The reasons for this phenomenon can be summed up in three ways: (1) numerous defect states in nanowire electrode lead to great charge trapping; (2) the enhanced interfacial charge carrier recombination through the large interface area between the

n-type nanowire electrode and CQDs; (3) the smaller hole diffusion length or extraction rate in CQDs layer enhances the charge recombination which offsets the contribution of photogenerated charge carriers to J_{SC} . What needs to pay special attention is that the value of hole mobility of PbS CQD has been found to be much smaller than its electron mobility [26]. How to effectively improve the hole mobility of PbS CQDs active layer to reduce recombination and improve hole collection efficiency in PbS CQDs layer is an urgent issue for CQDSCs. This issue settlement will be beneficial to elongate the carrier lifetime and fully harnesses great potential for the advance in the photovoltaic performance of CQDSCs. Unfortunately, scarcely related work has been reported nowadays.

Graphene oxide (GO) has been successfully employed as hole transport layer to improve the hole extraction rate from active layer to counter electrode in many typical solar cells such as polymer solar cells [27], perovskite solar cells [28], and CQDSCs due to its superior hole extraction efficiency [29–31]. It is very interesting that the surface of GO can also be chemically modified by special organic materials. Surface-modified GO can uphold the intrinsic hole transfer peculiarity of GO on the one hand and attenuate the hydrophilicity of GO in order to possibly allow for its good dispersibility in organic solvents on the other hand. Taking the well dispersed solvent of CQD into consideration, butylamine (BTA) is a good option to chemically modify the surface of GO.

Unlike the utilization of GO as a hole transport layer, we herein introduce the surface-modified GO using BTA by exploiting the bonding between the functional groups on the surface of GO and BTA to prepare BTA@GO/PbS-PbX₂ hybrid CQDs active layer in order to elevate the inherent hole mobility of CQDs layer. Here we deposit the CQDs active layer of PbS CQDSCs via one-step deposition strategy using BTA@GO/PbS-PbX₂ hybrid CQDs ink. It is found that the introduction of BTA@GO can build up a bulk nano-heterojunction architecture, which effectively improves the charge transfer rate and carrier mobility, extends the carriers lifetime and reduces the trap density of PbS-PbX₂ CQDs film. The BTA@GO/PbS-PbX₂ hybrid CQDs film-based relatively large-area (0.35 cm^2) CQDSCs shows a champion PCE of 11.7% with J_{SC} of 33.9 mA cm^{-2} , V_{OC} of 0.622 V and FF of 0.555. Compared to the PCE of 9.5% achieved by the PbS-PbX₂ CQDs film-based control device,

the efficiency is increased by 23.1%. In addition, the BTA@GO/PbS-PbX₂ hybrid CQDs film-based device exhibits good output and air storage stability.

2 Experimental

2.1 Materials

Oleic acid (OA, 90%), 1-octadecene (ODE, 90%), oleylamine (OLA, 70%), tetradecylphosphonic acid (TDPA, 97%), 1,2-ethanedithiol (EDT, 98%), hexamethyldisilathiane (TMS), lead bromide (PbBr₂, 95%), and poly(3,4-ethylenedioxythiophene)-poly(styrenesulfonate) (PEDOT:PSS) were purchased from Sigma-Aldrich. Lead (II) oxide (PbO, 99.5%), cadmium chloride (CdCl₂, 95%), ammonium acetate (NH₄Ac, 95%), *N,N*-dimethylformamide (DMF, 99.7%), octane (99%), butylamine (BTA, 99%), acetone (99.7%), methanol (99.7%), and toluene (99%) were purchased from Wako. Lead iodide (PbI₂, 99%) was purchased from Kanto Chemicals. Graphene oxide (GO, product number: XF002-1) was purchased from Nanjing XFNANO Materials. All chemicals were used without any purification.

2.2 Synthesis of PbS CQD

PbS CQD was synthesized by using our previously reported method [6]. Briefly, 6 mmol of PbO and 15 mmol of OA were dissolved in 50 mL of ODE by degassing the mixture at room temperature and 80 °C under vacuum for 0.5 and 2 h, respectively. Under nitrogen atmosphere, 630 μL TMS together with 10 mL ODE was quickly injected into the lead precursor at 85 °C. When the obtained PbS CQD solution was cooled to 70 °C, CdCl₂-TDPA-OLA halide passivation solution was injected. After the mixture solution was cooled to room temperature, PbS CQD was purified by acetone/methanol mixture solution. The obtained PbS CQD precipitate was dried by nitrogen flow and diluted in octane (100 mg mL⁻¹).

2.3 Preparation of BTA@GO Solution

20 mL BTA containing monolayer GO sheet (0.1–0.3 mg mL⁻¹) was sonicated for about 1 h in an ultrasonic bath, and then the mixture was stirred under reflux

condition at 60 °C for 24 h. After that, a well-dispersed BTA@GO solution was obtained.

2.4 Preparation of PbS CQDs Ink

The PbS CQDs ink was prepared by a reported solution-phase ligand-exchange method [16, 17]. Briefly, 12 mL OA-capped PbS (PbS-OA) CQD octane solution (20 mg mL⁻¹) was dropwise added into 20 mL DMF solution which dissolves 0.1 M PbI₂, 0.04 M PbBr₂ and 0.06 M NH₄Ac with vigorous stirring. This mixture was continued to stir for 5 min after PbS CQD octane solution dropping out. The upper octane phase was removed, and the DMF phase was washed for three times with octane. Then the PbX₂ (X = I, Br)-capped PbS (PbS-PbX₂) CQDs were precipitated from DMF by adding 15 mL of toluene and were collected by centrifugation at 7500 rpm for 5 min. The obtained PbS-PbX₂ CQD precipitate was then dried in a vacuum oven at room temperature for 30 min and dispersed in BTA or BTA@GO solution.

2.5 Photovoltaic Device Fabrication

The FTO/TiO₂ substrate was prepared following a published method [17]. The substrate was annealed again and further treated with oxygen plasma for 10 min before use. The CQDs active layer was deposited onto FTO/TiO₂ substrate by a one-step spinning 120 μL CQDs ink at 2500 rpm for 1 min. The obtained FTO/TiO₂/CQDs film was dried in vacuum oven at room temperature for 3 h. Subsequently, two PbS-EDT CQD layers (about 110 nm) were deposited onto FTO/TiO₂/CQDs film by a layer-by-layer spin-coating deposition method. Finally, Au top electrode was thermally evaporated onto the PbS-EDT CQDs film. Four identical solar cells are integrated on each substrate with an active area of 0.35 cm².

2.6 Characterization

Fourier transform infrared (FTIR) spectra of GO, BTA and BTA@GO were performed using a Thermo Scientific Nicolet 6700 FTIR spectrometer. Transmission electron microscope (TEM) images of CQDs and GO were determined by JEOL JEM-2100F. Scanning electron microscope (SEM) images were examined using JEOL

JSM-6340. Atomic force microscope (AFM) images were measured using SHIMADZU SPM-9700. Photoelectron yield spectroscopy (PYS) was obtained by Bunkoukeiki BIP-KV205. Absorption spectrum was captured by using a JASCO V-670 spectrophotometer. Time-resolved transient absorption (TA) measurement was carried out on a fs-TA system. PbS CQD films for TA measurement were sealed into a transparent quartz cuvette (size: $60 \times 10 \times 40 \text{ mm}^3$) filled with N_2 gas, and the excitation positions of sample were moved during the measurement using a XY translational stage. The microwave photoconductivity decay (μ -PCD) measurement was carried out on JEIDA-53 with a UV 349 nm excitation light and a differential μ -PCD (26 GHz) detection method. The current density–voltage (J – V) curve of device was obtained using a Keithley 2400 digital source meter in the dark and under one-sun irradiation ($\text{AM } 1.5 \text{ G } 100 \text{ mW cm}^{-2}$). The incident photon to current conversion efficiency (IPCE) measurement was recorded by using CEP-2000SRR, Bunko Keiki with a 300 W Xe lamp. Electrochemical impedance spectroscopy (EIS) of solar cell device was obtained by using SP-300 (BioLogic) impedance analyzer with a bias of 0.55 V (amplitude 10 mV).

3 Results and Discussion

3.1 Fabrication of BTA@GO/PbS-PbX₂ Hybrid CQDs Ink

In order to effectively disperse the GO sheet without aggregation or precipitation, BTA was first used to chemically modify the surface of the GO sheet and obtain the uniformly dispersed BTA@GO/PbS hybrid CQDs ink. As it is known to all, the surface of GO sheet has many functional groups, such as carboxyl and hydroxyl [32]. Among them, carboxyl group can readily react with the amide unit in the BTA to make a stable BTA@GO solution as illustrated in Fig. 1a. After a brief ultrasonic treatment for the GO and BTA complexes, a stable BTA@GO dispersion is formed. Figure 1b shows the photograph of dispersions of GO in BTA at 0.3 mg mL^{-1} concentration. The chemical changes occurring between GO with BTA can be observed by FTIR in Fig. 1c. For BTA, the peak at 2962 cm^{-1} is assigned to the asymmetric CH_3 stretch of BTA. The peaks at 2935 and 2871 cm^{-1} which belong to the C–H stretching vibrations of the hydrocarbon chains of the BTA. The strong peak at around 3300 cm^{-1} is

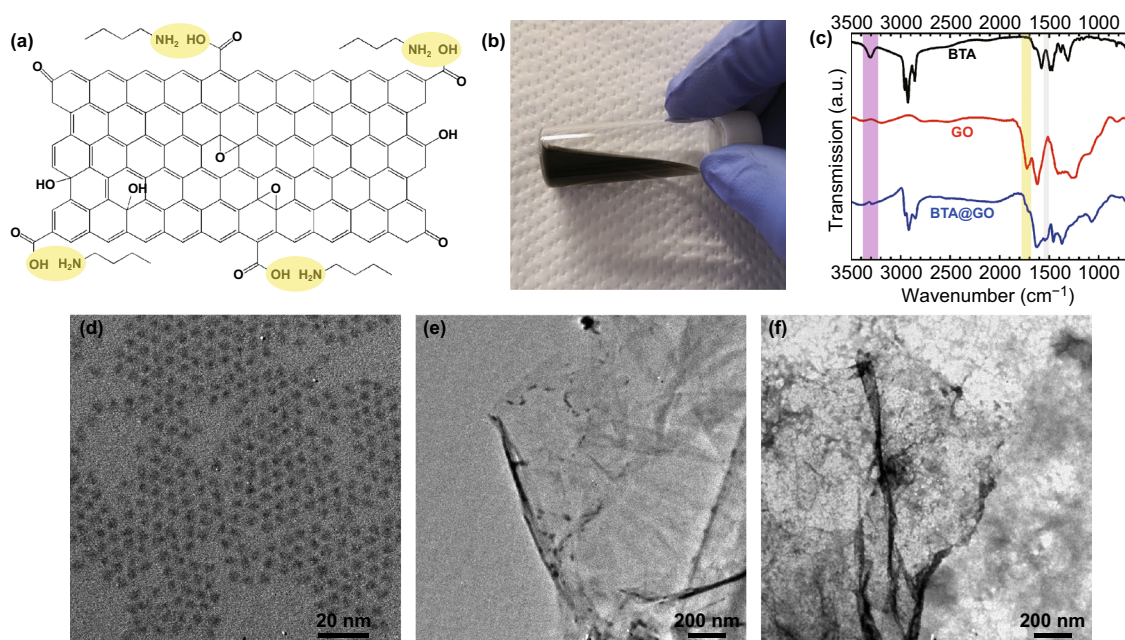


Fig. 1 **a** Chemical structure of the GO and the formation mechanism of BTA@GO. **b** Photograph of BTA@GO solution (0.3 mg mL^{-1}). **c** FTIR spectra of BTA, GO and BTA@GO on glass/Au substrate. **d** TEM image of colloidal PbS-OA CQD. TEM images of **e** BTA@GO and **f** PbS-PbX₂ CQD coupled with BTA@GO, the scale bar is 200 nm

assigned to the N–H stretching of BTA. For bare GO, the peak at around 3120–3500 cm^{-1} attributes to the –OH group (H bonded), C=O stretching of carboxyl group at 1715 cm^{-1} and carbonyl group at 1620 cm^{-1} , C–OH bond stretch at 1250 cm^{-1} , and C–O bond stretching of the epoxy group at from 900 to 1150 cm^{-1} can identify the types of functional groups on the surface of GO. Clearly, in BTA@GO, the presence of three new peaks at 2955, 2918, and 2850 cm^{-1} belongs to C–H stretching vibrations of the hydrocarbon chains of the BTA anchored onto the GO surface. In addition, the significant intensity decrements of the peaks at 1715 and 3300 cm^{-1} and the generation of new peak around 1530 cm^{-1} which is associated with the C–N stretching and N–H bending of secondary amides in BTA@GO confirm the formation of new amide bond in BTA@GO (Fig. S1). TEM images of PbS-OA CQD, BTA@GO, PbS-PbX₂ CQD, and BTA@GO/PbS-PbX₂ hybrid CQD are shown in Figs. 1d–f and S2. It is confirmed that the CQD-CQD distance for PbS-PbX₂ CQD is narrowed after solution-state ligand exchange comparing with PbS-OA CQD.

3.2 Photogenerated Carrier Transfer in BTA@GO/PbS-PbX₂ Hybrid CQDs Film

To clearly investigate the energy level matching degree between the surface-modified GO named BTA@GO and PbS-PbX₂ CQDs or PbS-EDT CQDs, the highest occupied molecular orbital (HOMO) positions of PbS-PbX₂ CQDs

and BTA@GO are measured by using PYS. We find that the color of GO films is different when they are deposited in different solvents. The GO film deposited by using H₂O@GO solution appears a brown color (Fig. S3a) which is the same as the color of original GO powder, and the film deposited by using BTA@GO solution shows a dark brown color (Fig. S3b). It is mainly caused by the changing of the functional groups on the GO surface [33, 34]. After BTA chemical treatment, the original carboxyl groups on GO can be converted to new amides which has been confirmed by FTIR (Figs. 1c and S1). This change affects not only the color of GO but also its HOMO level. The values of HOMO positions of H₂O@GO and BTA@GO are –5.22 and –5.19 eV, respectively (Fig. S3a, b). The values of HOMO positions of PbS-PbX₂ CQDs and PbS-EDT CQDs are –5.49 and –5.04 eV, respectively (Fig. S3c, d). It means that the photogenerated holes in PbS-PbX₂ CQDs layer which contract with or near BTA@GO tend to inject from PbS-PbX₂ CQDs to BTA@GO, and eventually fast transported through GO to PbS-EDT CQDs (Fig. 2b). In contrast, the photogenerated holes in PbS-PbX₂ CQDs layer which are far from BTA@GO should move to the interface of PbS-PbX₂/PbS-EDT layers via slow diffusion in PbS-PbX₂ CQDs layer. The optical bandgap of BTA@GO is approximately 1.85 eV (Fig. S3e), and the calculated LUMO level of BTA@GO is –3.34 eV which is much higher than the LUMO position of PbS-PbX₂ CQDs. This high-energy barrier can suppress the photogenerated electrons inject from PbS-PbX₂ CQDs to BTA@GO. The electrons in PbS-PbX₂ CQDs layer tend to move to the

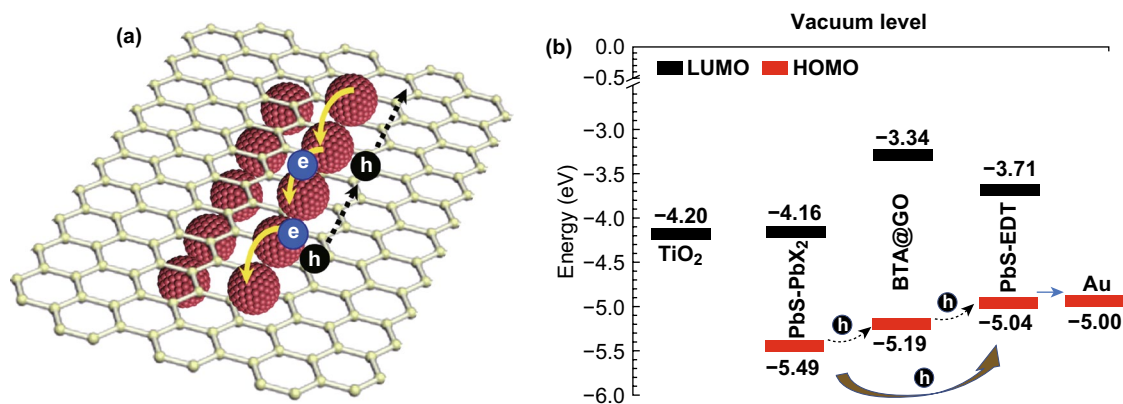


Fig. 2 **a** Schematic diagram of the charge transport process in the BTA@GO/PbS-PbX₂ hybrid CQDs film. **b** Schematic energy level diagram of the TiO₂, PbS-PbX₂ CQDs, BTA@GO, PbS-EDT CQDs, and Au

electron collection layer (TiO_2) under the driving force of the built-in electric field in the solar cell device. This consideration is then substantiated by measuring the photoexcited charge carrier transfer for PbS-PbX₂ and BTA@GO/PbS-PbX₂ CQD solid films using time-resolved TA spectroscopy.

TA and ground-state absorption spectra of PbS-OA, PbS-PbX₂, and BTA@GO/PbS-PbX₂ CQD films are shown in Figs. 3a–c and S4, respectively. It can be manifestly observed that both TA bleaching peak and ground-state absorption peak around 930 nm (1.33 eV) of the PbS-OA CQDs correspond to the lowest-energy excitons in the CQDs. For the CQD film prepared using the CQD ink after solution-phase ligand exchange, due to the narrowed CQD-CQD distance and the enhanced coupling effect between PbS CQDs in the film, the TA bleaching peaks and optical absorption peaks for both of PbS-PbX₂ CQDs and BTA@GO/PbS-PbX₂ CQDs are slightly redshifted to 970 nm. In order to eliminate the interference of Auger recombination and obtain large signal-to-noise ratio, a weak excitation fluence of $6 \mu\text{J cm}^{-2}$

is adopted in the TA measurement (Fig. S5). In Figs. 3d and S6, compared with PbS-OA CQDs (probe wavelength 930 nm), obviously fast TA bleaching signal decay (probe wavelength 970 nm) for both PbS-PbX₂ CQDs and BTA@GO/PbS-PbX₂ CQDs films can be observed on the time scale of 1 ns. The fast TA bleaching signal decay indicates charge carriers transfer occurring in those CQD films. The TA decay curves can be well fitted by biexponential decay with a constant signal, and the fitting results are shown in Table 1. The faster decay is contributed to charge carrier trapping of PbS CQDs (parameters are represented as τ_{tr}). The relatively slower decay process corresponds to the charge carrier transfer behavior between CQD-CQD and CQD-BTA@GO (parameters are represented as τ_{ct}). The values of carrier transfer time constant τ_{ct} for PbS-PbX₂ CQDs film and BTA@GO/PbS-PbX₂ hybrid CQDs film are about 243 ± 4 and 180 ± 3 ps, respectively. Also, the corresponding carrier transfer rate constants ($k_{\text{ct}} = 1/\tau_{\text{ct}}$) of PbS-PbX₂ CQDs film and BTA@GO/PbS-PbX₂ hybrid CQDs film are 4.1×10^9

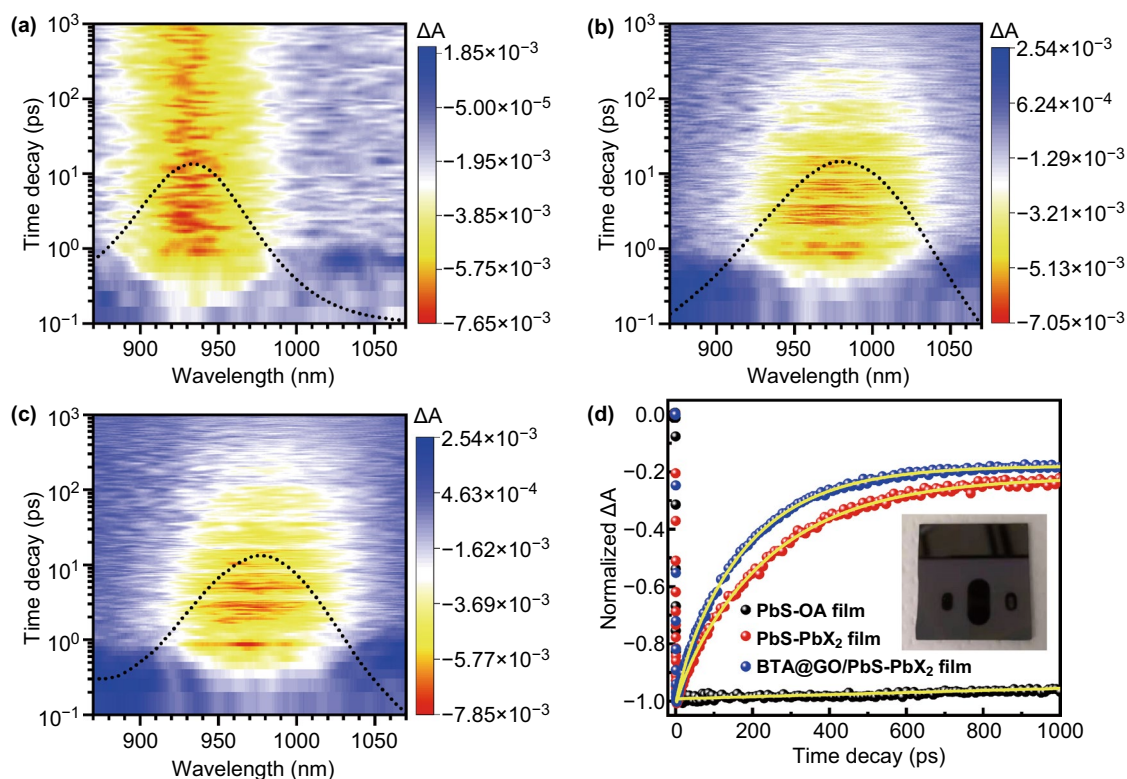


Fig. 3 Comparison of the TA decays of PbS-OA CQDs film, PbS-PbX₂ CQDs film and BTA@GO/PbS-PbX₂ hybrid CQDs film. **a–c** TA and ground-state absorption spectra for PbS-OA, PbS-PbX₂ and BTA@GO/PbS-PbX₂ CQD films. The excitation wavelength is 470 nm with a pulse fluence of $20 \mu\text{J cm}^{-2}$. **d** Normalized absorption changes (ΔA) of those films; the films are excited by 470 nm pulse with a fluence of $6 \mu\text{J cm}^{-2}$. The inset is the photograph of BTA@GO/PbS-PbX₂ CQDs film, and the shadow of the phone used to take photo is reflected in the mirror-like surface of the CQDs film

Table 1 Fitted time constants and the corresponding proportionality constants obtained from the TA decay curves of PbS-PbX₂ CQDs film and BTA@GO/PbS-PbX₂ hybrid CQDs film as shown in Fig. 3d

Sample	A _{tr}	τ _{tr}	A _{ct}	τ _{ct}	A ₀
PbS-OA	–	–	–	–	0.998 ± 0.002 (100%)
PbS-PbX ₂	–0.041 ± 0.006 (4.0%)	21 ± 6 (ps)	–0.758 ± 0.006 (74.6%)	243 ± 4 (ps)	–0.217 ± 0.002 (21.4%)
BTA@GO/PbS-PbX ₂	–0.033 ± 0.004 (3.4%)	23 ± 3 (ps)	–0.802 ± 0.005 (80.0%)	180 ± 3 (ps)	–0.167 ± 0.003 (16.6%)

and $5.6 \times 10^9 \text{ s}^{-1}$, respectively. It means that charge carrier transfer between CQDs in the film prepared using the BTA@GO/PbS-PbX₂ hybrid CQDs ink is faster than that in the film deposited using the PbS-PbX₂ CQDs ink due to the contribution of the charge carrier transfer process between CQD and BTA@GO. This result reflects that PbS-PbX₂ CQDs can closely couple with BTA@GO in the BTA@GO/PbS-PbX₂ hybrid CQDs film. The carrier transfer rate from PbS-PbX₂ CQD to BTA@GO can be estimated by Eq. 1:

$$k_{\text{CQD-BTA@GO}} = k_{\text{avg}} - k_{\text{CQD-CQD}} \quad (1)$$

where k_{avg} is carrier transfer rate constant (k_{ct}) of BTA@GO/PbS-PbX₂ CQDs, $k_{\text{CQD-CQD}}$ is carrier transfer rate constant between CQD-CQD, and $k_{\text{CQD-BTA@GO}}$ is carrier transfer rate constant between CQD and BTA@GO. The calculated value of $k_{\text{CQD-BTA@GO}}$ is $1.5 \times 10^9 \text{ s}^{-1}$, and the percentage of carrier transfer between CQD-BTA@GO is about 27% ($k_{\text{CQD-BTA@GO}}/k_{\text{avg}}$). This means that about 27% of photogenerated holes can transport through BTA@GO channel in BTA@GO/PbS-PbX₂ hybrid CQDs film. The larger carrier transfer rate of BTA@GO/PbS-PbX₂ CQDs film will reduce the probability of charge carrier recombination which is confirmed by the EIS results (see Fig. 6b and Table S5) of solar

cell devices. These results are beneficial for improving the V_{OC} and FF of CQDSCs device.

Moreover, the carrier mobility and trap density of the CQDs film were also evaluated by using the space-charge-limited current (SCLC) method [35]. The structure and SEM image of the hole-only device (ITO/PEDOT:PSS/PbS CQDs/PEDOT:PSS/Au) are shown in Figs. 4 and S7, respectively. The typical dark current density–voltage (J – V) curves were obtained from SCLC measurement as shown in Fig. 4a, b, which can be divided into three regions: Child’s regime ($J \propto V^2$) at high bias voltage, Ohmic linear regime ($J \propto V$) at the low bias voltage, and nonlinear trap-filled regime between them [36]. The carrier mobility (μ) in CQDs film can be calculated by fitting the J – V curve at Child’s regime with a Mott-Gurney law [37–40]:

$$J = \frac{9}{8} \epsilon_0 \epsilon \mu \frac{V^2}{L^3} \quad (2)$$

where J is the current density, ϵ_0 is the permittivity under vacuum, ϵ is the relative dielectric constant of PbS CQDs (about 14.5) [41], V is the applied voltage, and L is the thickness of PbS CQDs layer (about 330 nm). The calculated

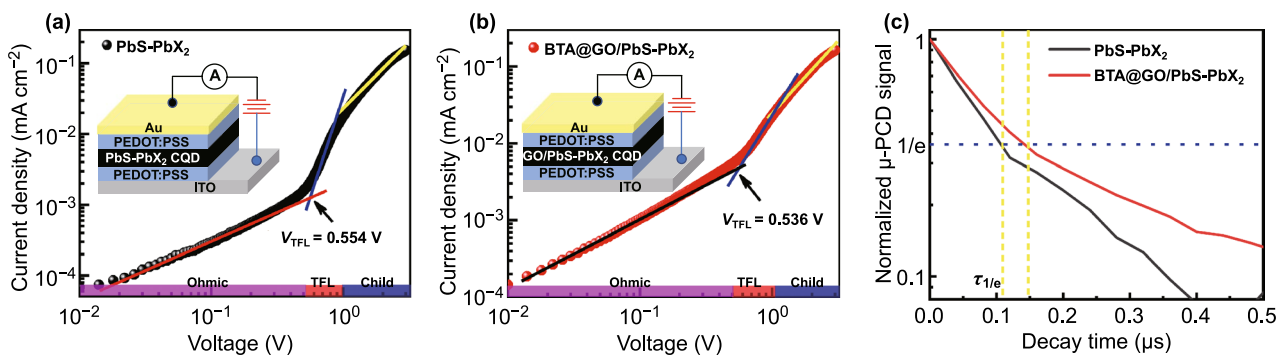


Fig. 4 Dark J – V curves of hole-only devices based on PbS-PbX₂ CQDs film **a** without and **b** with BTA@GO. **c** Normalized μ -PCD decay curves for the PbS-PbX₂ CQDs film and BTA@GO/PbS-PbX₂ hybrid CQDs film. The value of the blue short-dash line is $1/e$, and the value of the yellow short-dash line is $\tau_{1/e}$ of carrier decay time, which are approximately 0.11 μs and 0.15 μs for the PbS-PbX₂ CQDs film and BTA@GO/PbS-PbX₂ hybrid CQDs film, respectively

hole mobility of BTA@GO/PbS-PbX₂ hybrid CQDs film is 0.0030 cm² V⁻¹ s⁻¹, about 30% improvement as compared with hole mobility of 0.0023 cm² V⁻¹ s⁻¹ for the PbS-PbX₂ CQDs film. The introduction of BTA@GO can more effectively improve the hole mobility in the CQDs film. By the benefit from the additional BTA@GO charge transport channel, the BTA@GO/PbS-PbX₂ hybrid CQDs film exhibits the higher carrier mobility than that of the control PbS-PbX₂ CQDs film, which is consistent with the result of TA measurement. In addition, the trap-filled limit voltage (V_{TFL}) can be extracted from the intersection of the curves between the trap-filled region and Ohmic linear region, which is determined by the trap density (n_{trap}) in the device [42]:

$$V_{\text{TFL}} = \frac{en_{\text{trap}}L^2}{2\epsilon_0\epsilon} \quad (3)$$

The values of V_{TFL} for PbS-PbX₂ CQDs film and BTA@GO/PbS-PbX₂ hybrid CQDs film are 0.554 and 0.536 V, respectively. The calculated value of hole trap density for BTA@GO/PbS-PbX₂ hybrid CQDs film is 7.89×10^{15} cm⁻³, which is lower than that of PbS-PbX₂ CQDs solid film (8.16×10^{15} cm⁻³). This confirms that the bulk nano-heterojunction architectural for BTA@GO/PbS-PbX₂ hybrid CQDs film can effectively passivate the trap state of PbS CQDs film [43], which is consistent with the result of TA measurement. Meanwhile, the free carrier lifetime ($\tau_{1/e}$) in the CQDs film obtained from microwave photoconductivity (μ -PCD) decay measurement is increased from 0.11 to 0.15 μ s after BTA@GO introducing (Fig. 4c). The conductivity (σ) of the CQDs film is also measured (Fig. S8), and the evaluated σ values for PbS-PbX₂ and BTA@GO/PbS-PbX₂ CQD films are 5.18×10^{-4} and 6.16×10^{-4} S m⁻¹, respectively. It indicates that there is some improvement in the carrier transport property of PbS-PbX₂ CQD film after BTA@GO introducing. To put it from another angle, the BTA@GO-coupled CQDs film provides an effective carrier transport channel for enhanced carrier transport, which is beneficial for achieving higher J_{SC} and V_{OC} of CQDSCs.

3.3 Photovoltaic Performance of BTA@GO/PbS-PbX₂ Hybrid CQDs Film-Based Solar Cells

The efficient charge carrier transfer, enhanced carrier mobility and conductivity, as well as the extended free carrier lifetime in BTA@GO/PbS-PbX₂ hybrid CQDs film are beneficial for thorough understanding of the photovoltaic

performance of CQDSCs. A bulk nano-heterojunction device structure of FTO/TiO₂/BTA@GO@PbS-PbX₂/PbS-EDT/Au was designed and fabricated using BTA@GO/PbS-PbX₂ hybrid CQDs ink as schematically illustrated in Fig. 5a, and the AFM images of PbS-PbX₂ and BTA@GO/PbS-PbX₂ CQD films and a cross-section SEM image of the device are presented in Figs. S9 and 5b, respectively. We fabricated and measured 12 devices for each type of the CQDSCs based on PbS-PbX₂ CQDs film and BTA@GO/PbS-PbX₂ hybrid CQDs film to ensure the repeatability of the hybrid inks and device fabrication. Figure 5c provides the J - V curves of the two type CQDSCs devices under one-sun (AM1.5G 100 mW cm⁻²) illumination. Table 2 shows the values of the performance parameters for those devices. The champion device (active area is 0.35 cm²) employing BTA@GO/PbS-PbX₂ hybrid CQDs film achieved a PCE of 11.7%, with J_{SC} , V_{OC} , and FF of 33.9 mA cm⁻², 0.622 V, and 55.5%, respectively. Additionally, there is no hysteresis in the device (Fig. S10 and Table S1). Compared to the control device which was fabricated with PbS-PbX₂ CQDs film (PCE of 9.5%), all performance parameters of BTA@GO/PbS-PbX₂ hybrid CQDs film-based CQDSCs were improved and the PCE was increased by 23%. Just as above mentioned, the charge transfer rate, carrier mobility and conductivity for the BTA@GO/PbS-PbX₂ hybrid CQDs film are larger than those of the controlled PbS-PbX₂ CQDs film. Thus, compared to PbS-PbX₂ CQDs film-based device, the larger J_{SC} of BTA@GO/PbS-PbX₂ hybrid CQDs film-based CQDSCs should be caused by the faster charge transfer rate, larger carrier mobility, and higher carrier extraction efficiency. The incident photon-to-current conversion efficiency (IPCE) spectrum and the calculated J_{SC} from the IPCE of the BTA@GO/PbS-PbX₂ hybrid CQDs film-based CQDSCs are shown in Fig. 5d. The calculated J_{SC} (32.3 mA cm⁻²) is close to the value obtained from above J - V measurements. We optimized the adding amount of BTA@GO in the CQD inks for CQDSCs (Fig. 5e). The J_{SC} , V_{OC} , and FF of the devices firstly improve and then reduce with the optimized 0.2 mg mL⁻¹ concentration of GO in the ink (Fig. S11 and Table S2). Excessive adding of BTA@GO may enhance the recombination in the device. We also optimized the thickness of CQDs layer by changing the concentration of CQD inks for CQDSCs (Fig. 5f). As shown in Fig. S12, with the increases in CQD inks concentration, the thickness of CQDs film increases. The J_{SC} of the both devices first grow sharply and then reduce slightly as the

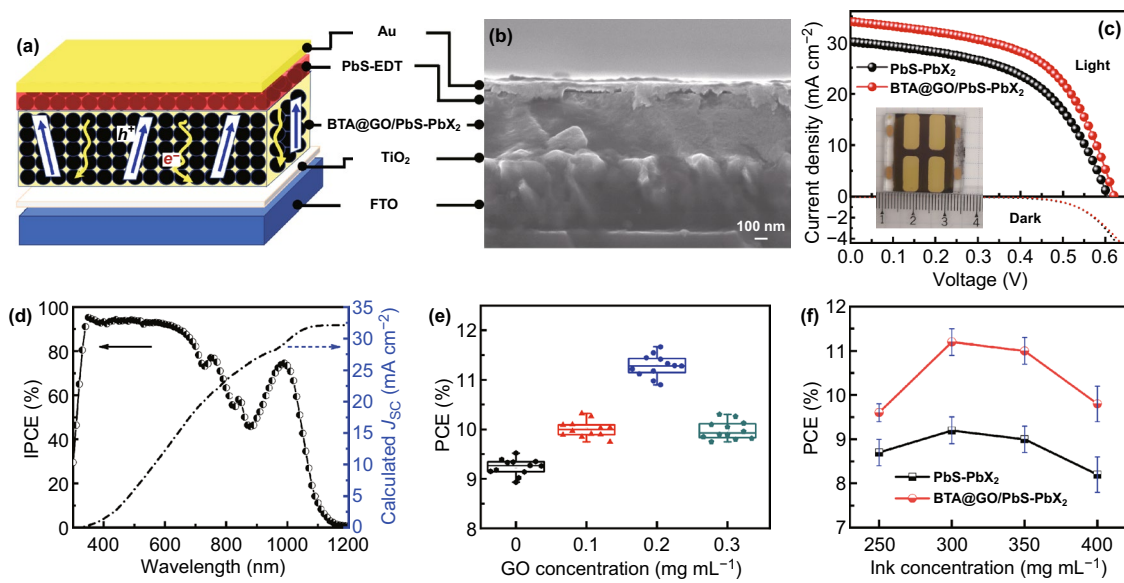


Fig. 5 **a** Schematic diagram of the bulk nano-heterojunction structure CQDSCs with BTA@GO/PbS-PbX₂ hybrid CQDs film. **b** Cross-sectional SEM image of the CQDSCs device. **c** *J*-*V* curves of CQDSCs based on the controlled PbS-PbX₂ CQDs film and the BTA@GO/PbS-PbX₂ hybrid CQDs film (the concentration of GO in CQDs ink is 0.2 mg mL⁻¹). The inset is the photograph of CQDSCs device. **d** IPCE spectrum and integrated *J*_{SC} of BTA@GO/PbS-PbX₂ CQDSCs. **e** Statistical distribution of PCEs for PbS-PbX₂ CQDSCs devices with the different concentrations of GO in CQD inks from 0 to 0.3 mg mL⁻¹. **f** Statistical distribution of PCEs for PbS-PbX₂ CQDSCs devices which are fabricated by different concentrations of CQD inks from 250 to 400 mg mL⁻¹

Table 2 Performance parameters of CQDSCs based on PbS-PbX₂ CQDs film and BTA@GO/PbS-PbX₂ hybrid CQDs film. Light intensity for the measurement is one-sun

Devices	<i>J</i> _{SC} (mA cm ⁻²)	<i>V</i> _{OC} (V)	FF (%)	PCE (%)
PbS-PbX ₂	30.1 ± 0.7 (30.1)	0.600 ± 0.008 (0.606)	51.3 ± 1.3 (52.3)	9.2 ± 0.3 (9.5)
BTA@GO/PbS-PbX ₂	33.2 ± 0.8 (33.9)	0.617 ± 0.007 (0.622)	54.5 ± 1.2 (55.5)	11.3 ± 0.4 (11.7)

The devices were measured under air at 20 °C with humidity of 45%. The values in parentheses are the parameters for the champion devices

thickness increases, but sacrificing *V*_{OC} and FF (Fig. S12, Tables S3 and S4). It indicates that although thick CQDs layer can absorb more light (see Fig. S13) which benefits to generate charge carriers, the performance of the device is also constrained by the limit of carrier diffusion length and the increased trap density [16, 44].

As we discussed above, the introduction of BTA@GO is beneficial for extracting holes from PbS CQD and provides a fast charge transport channel to carry the holes to the PbS-EDT hole-selective layer. This additional charge transport path and the bulk nano-heterojunction architecture are beneficial to reduce the probability of interfacial-assisted carrier recombination in CQDs layer which is caused by the trap states of PbS CQDs, and it is confirmed by the result

of SCLC measurement (Fig. 4). The suppressed interfacial-assisted carrier recombination can weaken its contribution to *V*_{OC} deficit of the CQDSCs device. Diode ideality factor (*n*) is an important parameter of solar cells which can be used to reveal the carrier recombination process in the device. When the value of *n* approaches 1, it indicates that the carrier recombination process in solar cells device is mainly determined by charge carrier band-to-band directly recombination. On the contrary, when the value of *n* is much greater than unity (1 < *n* < 2), the interfacial-assisted recombination instead of the competition with band-to-band recombination mainly dominates the carrier recombination process in the device. We evaluate the diode ideality factor of the PbS-PbX₂ CQDs film and BTA@GO/PbS-PbX₂ hybrid CQDs

film-based CQDSCs from a slope in V_{OC} plotted against the logarithm of the J_{SC} based on Eq. 4 [17]:

$$V_{OC} \propto \frac{nk_B T}{q} \ln(J_{SC}) \quad (4)$$

where n , k_B , T , and q are the diode ideality factor, Boltzmann constant, temperature, and elementary charge, respectively. As shown in Fig. 6a, the estimated values of n are 1.56 and 1.31 for PbS-PbX₂ CQDs film and BTA@GO/PbS-PbX₂ hybrid CQDs film-based CQDSCs, respectively. The smaller n for BTA@GO/PbS-PbX₂ hybrid CQDs film-based CQDSCs reflects the reduced interfacial-assisted recombination in the BTA@GO/PbS-PbX₂ hybrid CQDs film layer comparing with the CQDs film without BTA@GO. It can be concluded from the above results that the introduction of BTA@GO into PbS-PbX₂ CQDs film can significantly improve the carrier transport, diminish the recombination in CQDs film layer, and therefore enhance the V_{OC} and PCE.

So as to reveal the kinetic mechanism of the CQDSCs, EIS has been performed at negative applied bias. Figure 6b shows the Nyquist plots of CQDSCs based on PbS-PbX₂ CQDs film and BTA@GO/PbS-PbX₂ hybrid CQDs film under dark with 0.55 V applied bias. The series resistance (R_s), recombination resistance (R_{rec}), and chemical capacitance (C) of devices can be obtained (Table S5) by analyzing the EIS spectra with the equivalent circuits plotted in Fig. 6c. The fitted value of R_s for BTA@GO/PbS-PbX₂ hybrid CQDs

film-based device (12.3 Ω) is found to be smaller than that for PbS-PbX₂ CQDs film-based device (12.9 Ω), this may be caused by the reduced resistance of the BTA@GO/PbS-PbX₂ hybrid CQDs film. The R_{rec} of the device attributes to the sum of the low and intermediate frequency resistances. Compared with the PbS-PbX₂ CQDs film-based CQDSCs (1165 Ω), a larger R_{rec} is obtained as 1411 Ω for BTA@GO/PbS-PbX₂ hybrid CQDs film-based device. The value of carrier recombination rate constant (k_{rec}) can be estimated by $k_{rec}=1/(R \times C)$ and the corresponding k_{rec} values for the PbS-PbX₂ CQDs film and BTA@GO/PbS-PbX₂ hybrid CQDs film-based CQDSCs are 5.7×10^4 and 3.9×10^4 s⁻¹, respectively. The smaller R_s as well as smaller k_{rec} values for BTA@GO/PbS-PbX₂ hybrid CQDs film-based CQDSCs device indicate the improved carrier transport and reduced charge recombination in the device, which is favorable for improving the FF and V_{OC} of CQDSCs.

The stability is one of the important performance indicators of CQDSCs. The stable output curves of PCE of CQDSCs devices with and without BTA@GO as a function of time at the maximum output power condition were measured as shown in Fig. 7a. A stabilized output PCE of 11.5% at maximum power point (J_{max} of 25.6 mA cm⁻² and V_{max} of 0.450 V) is achieved for the CQDSCs device based on BTA@GO/PbS-PbX₂ hybrid CQDs film, which is higher

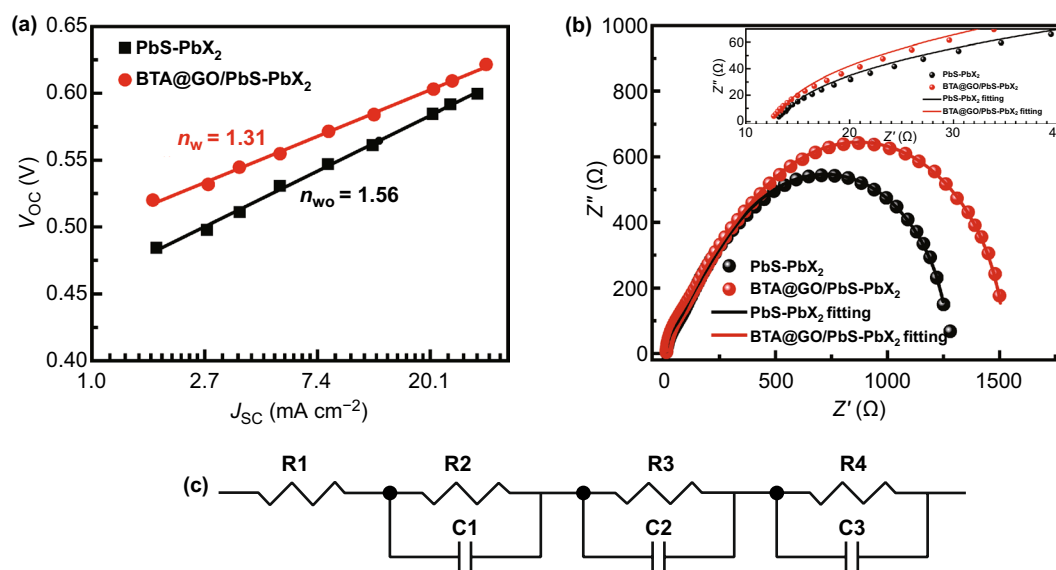


Fig. 6 **a** V_{OC} plotted against the logarithm of J_{SC} in the CQDSCs device with and without BTA@GO. **b** Nyquist plots of PbS-PbX₂ CQDs film and BTA@GO/PbS-PbX₂ hybrid CQDs film-based CQDSCs in dark with 0.55 V applied bias, and the solid curves are the fitting results by using the equivalent circuit plotted in **c**. **c** Equivalent circuit of CQDSCs device

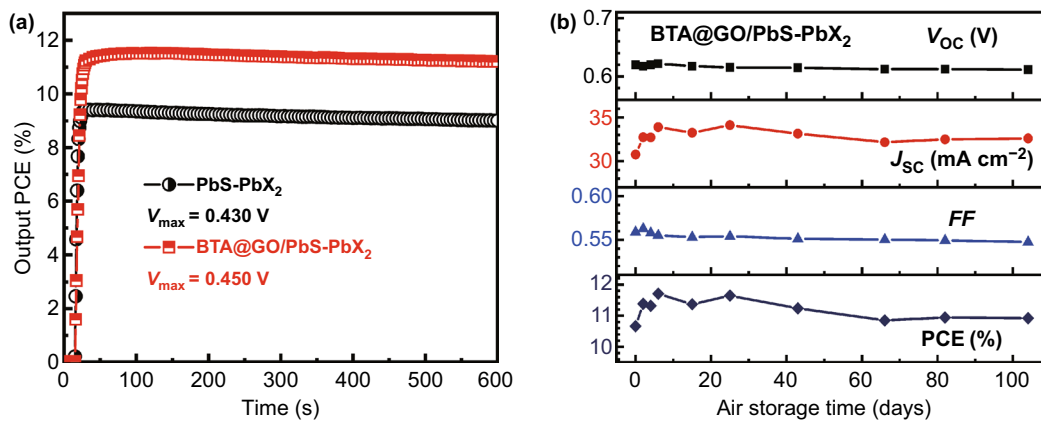


Fig. 7 **a** Stable output test of PbS-PbX₂ CQDs film and BTA@GO/PbS-PbX₂ hybrid CQDs film-based CQDSCs at maximum output power condition which were measured under AM1.5 G 100 mW cm⁻² light soaking in air. **b** Air storage stability of the BTA@GO/PbS-PbX₂ hybrid CQDs film-based CQDSCs with indoor relative humidity of 40–65%

and more stable than that of PbS-PbX₂ CQDs film-based device (9.4%, at J_{\max} of 21.9 mA cm⁻² and V_{\max} of 0.430 V). Thus, a small amount of BTA@GO adding can effectively improve the light-soaking stability of CQDSCs device. The long-term stability of BTA@GO/PbS-PbX₂ hybrid CQDs film-based CQDSCs was also investigated. The device was stored and tested in air with the humidity of 40–65%. As shown in Fig. 7b, the BTA@GO/PbS-PbX₂ hybrid CQDs film-based CQDSC exhibits good air storage stability for over 105 days, and the photovoltaic performance of the device was increased at the first 6 days. With storage time going on, the V_{oc} and FF of the device are slightly reduced which may be caused by the desorption of EDT from PbS CQDs surface in PbS-EDT layer in turn changed the energy level and trap density of PbS-EDT layer [45, 46]. Finally, the PCE of BTA@GO/PbS-PbX₂ hybrid CQDs film-based CQDSC retained about 93% of its peak value after 105 days, from 11.7 to 10.9%.

4 Conclusions

In summary, we artfully use the BTA-modified GO in the BTA@GO/PbS-PbX₂ hybrid CQDs ink to build a bulk nano-heterojunction architecture CQDSCs. The introduction of BTA@GO provides effective carrier transport channel which improves the charge transfer rate, carrier mobility, and conductivity, as well as the carrier lifetime of PbS-PbX₂ CQDs film. The bulk nano-heterojunction architecture can

reduce the carrier recombination rate and improve the carrier extraction in the device. Combined those advantages, all of the performance parameters of CQDSCs are enhanced. A stable output and air storage relatively large active area (0.35 cm²) BTA@GO/PbS-PbX₂ hybrid CQDs film-based CQDSC with a champion PCE of 11.7% was obtained, and the PCE shows a marked increase (23.1%) compared with the PbS-PbX₂ CQD-based CQDSCs. Our results suggest that improving the hole mobility of CQDs active layer and the bulk nano-heterojunction architecture is promising to further improve the performance of CQDSCs in future.

Acknowledgements This research was supported by the Japan Science and Technology Agency (JST) CREST program, Beijing Advanced Innovation Center for Future Urban Design, Beijing University of Civil Engineering and Architecture (Grant UDC2018031121), and the MEXT KAKENHI (Grant 17H02736). G.W. acknowledges the Natural Science Foundation of Shaanxi Province (2019JQ-423), the Fundamental Research Funds for the Central Universities (GK201903053), and Key Lab of Photovoltaic and Energy Conservation Materials, Chinese Academy of Sciences (No. PECL2019KF019) for financial support.

Open Access This article is licensed under a Creative Commons Attribution 4.0 International License, which permits use, sharing, adaptation, distribution and reproduction in any medium or format, as long as you give appropriate credit to the original author(s) and the source, provide a link to the Creative Commons licence, and indicate if changes were made. The images or other third party material in this article are included in the article's Creative Commons licence, unless indicated otherwise in a credit line to the material. If material is not included in the article's Creative Commons licence and your intended use is not permitted by statutory

regulation or exceeds the permitted use, you will need to obtain permission directly from the copyright holder. To view a copy of this licence, visit <http://creativecommons.org/licenses/by/4.0/>.

Electronic supplementary material The online version of this article (<https://doi.org/10.1007/s40820-020-00448-8>) contains supplementary material, which is available to authorized users.

References

1. Y. Zhang, G. Wu, F. Liu, C. Ding, Z. Zou, Q. Shen, Photo-excited carrier dynamics in colloidal quantum dot solar cells: insights into individual quantum dots, quantum dot solid films and devices. *Chem. Soc. Rev.* **49**, 49–84 (2020). <https://doi.org/10.1039/c9cs00560a>
2. R. Ahmed, L. Zhao, A.J. Mozer, G. Will, J. Bell, H. Wang, Enhanced electron lifetime of CdSe/CdS quantum dot (QD) sensitized solar cells using ZnSe core–shell structure with efficient regeneration of quantum dots. *J. Phys. Chem. C* **119**(5), 2297–2307 (2015). <https://doi.org/10.1021/jp510339z>
3. J. Tang, K.W. Kemp, S. Hoogland, K.S. Jeong, H. Liu et al., Colloidal-quantum-dot photovoltaics using atomic-ligand passivation. *Nat. Mater.* **10**(10), 765–771 (2011). <https://doi.org/10.1038/nmat3118>
4. Y. Cao, A. Stavrinadis, T. Lasanta, D. So, G. Konstantatos, The role of surface passivation for efficient and photostable PbS quantum dot solar cells. *Nat. Energy* **1**, 16035 (2016). <https://doi.org/10.1038/nenergy.2016.35>
5. X. Zhang, J. Zhang, D. Phuyal, J. Du, L. Tian et al., Inorganic CsPbI₃ perovskite coating on PbS quantum dot for highly efficient and stable infrared light converting solar cells. *Adv. Energy Mater.* **8**(6), 1702049 (2018). <https://doi.org/10.1002/aenm.201702049>
6. N. Nakazawa, Y. Zhang, F. Liu, C. Ding, K. Hori et al., The interparticle distance limit for multiple exciton dissociation in PbS quantum dot solid films. *Nanoscale Horiz.* **4**(2), 445–451 (2019). <https://doi.org/10.1039/C8NH00341F>
7. W. Chen, J.L. Zhong, J.Z. Li, N. Saxena, L.P. Kreuzer et al., Structure and charge carrier dynamics in colloidal PbS quantum dot solids. *J. Phys. Chem. Lett.* **10**(9), 2058–2065 (2019). <https://doi.org/10.1021/acs.jpclett.9b00869>
8. M.I. Hossain, W. Qarony, S. Ma, L. Zeng, D. Knipp, Y.H. Tsang, Perovskite/silicon tandem solar cells: from detailed balance limit calculations to photon management. *Nano-Micro Lett.* **11**, 58 (2019). <https://doi.org/10.1007/s40820-019-0287-8>
9. X. Ling, S. Zhou, J. Yuan, J. Shi, Y. Qian et al., 14.1% CsPbI₃ perovskite quantum dot solar cells via cesium cation passivation. *Adv. Energy Mater.* **9**(28), 1900721 (2019). <https://doi.org/10.1002/aenm.201900721>
10. C.H.M. Chuang, P.R. Brown, V. Bulović, M.G. Bawendi, Improved performance and stability in quantum dot solar cells through band alignment engineering. *Nat. Mater.* **13**(8), 796–801 (2014). <https://doi.org/10.1038/nmat3984>
11. S. Pradhan, A. Stavrinadis, S. Gupta, S. Christodoulou, G. Konstantatos, Breaking the open-circuit voltage deficit floor in PbS quantum dot solar cells through synergistic ligand and architecture engineering. *ACS Energy Lett.* **2**(6), 1444–1449 (2017). <https://doi.org/10.1021/acsenenergylett.7b00244>
12. Y.J. Gao, J.H. Zheng, W.J. Chen, L. Yuan, Z.L. Teh et al., Enhancing PbS colloidal quantum dot tandem solar cell performance by graded band alignment. *J. Phys. Chem. Lett.* **10**(19), 5729–5734 (2019). <https://doi.org/10.1021/acs.jpclett.9b02423>
13. X.K. Yang, L. Hu, H. Deng, K.K. Qiao, C. Hu et al., Improving the performance of PbS quantum dot solar cells by optimizing ZnO window layer. *Nano-Micro Lett.* **9**(2), 24 (2017). <https://doi.org/10.1007/s40820-016-0124-2>
14. F. Li, S. Zhou, J. Yuan, C. Qin, Y. Yang et al., Perovskite quantum dot solar cells with 15.6% efficiency and improved stability enabled by an α -CsPbI₃/FAPbI₃ bilayer structure. *ACS Energy Lett.* **4**(11), 2571–2578 (2019). <https://doi.org/10.1021/acsenenergylett.9b01920>
15. J. Yuan, X. Ling, D. Yang, F. Li, S. Zhou et al., Band-aligned polymeric hole transport materials for extremely low energy loss α -CsPbI₃ perovskite nanocrystal solar cells. *Joule* **2**(11), 2450–2463 (2018). <https://doi.org/10.1016/j.joule.2018.08.011>
16. M. Liu, O. Voznyy, R. Sabatini, F.P. Garcia de Arquer, R. Munir et al., Hybrid organic-inorganic inks flatten the energy landscape in colloidal quantum dot solids. *Nat. Mater.* **16**(2), 258–263 (2017). <https://doi.org/10.1038/nmat4800>
17. Y. Zhang, G. Wu, C. Ding, F. Liu, Y. Yao et al., Lead selenide colloidal quantum dot solar cells achieving high open-circuit voltage with one-step deposition strategy. *J. Phys. Chem. Lett.* **9**(13), 3598–3603 (2018). <https://doi.org/10.1021/acs.jpclett.8b01514>
18. G. Shi, A. Kaewprajak, X. Ling, A. Hayakawa, S. Zhou et al., Finely interpenetrating bulk heterojunction structure for lead sulfide colloidal quantum dot solar cells by convective assembly. *ACS Energy Lett.* **4**(4), 960–967 (2019). <https://doi.org/10.1021/acsenenergylett.9b00053>
19. M. Hao, Y. Bai, S. Zeiske, L. Ren, J. Liu et al., Ligand-assisted cation-exchange engineering for high-efficiency colloidal Cs_{1-x}FA_xPbI₃ quantum dot solar cells with reduced phase segregation. *Nat. Energy* **5**(1), 79–88 (2020). <https://doi.org/10.1038/s41560-019-0535-7>
20. M.C. Hanna, A.J. Nozik, Solar conversion efficiency of photovoltaic and photoelectrolysis cells with carrier multiplication absorbers. *J. Appl. Phys.* **100**(7), 074510 (2006). <https://doi.org/10.1063/1.2356795>
21. M.J. Choi, F.P. García de Arquer, A.H. Proppe, A. Seifitokaldani, J. Choi et al., Cascade surface modification of colloidal quantum dot inks enables efficient bulk homojunction photovoltaics. *Nat. Commun.* **11**(1), 103 (2020). <https://doi.org/10.1038/s41467-019-13437-2>
22. I.J. Kramer, D. Zhitomirsky, J.D. Bass, P.M. Rice, T. Topuria et al., Ordered nanopillar structured electrodes for depleted

- bulk heterojunction colloidal quantum dot solar cells. *Adv. Mater.* **24**(17), 2315–2319 (2012). <https://doi.org/10.1002/adma.201104832>
23. H. Wang, V. Gonzalez-Pedro, T. Kubo, F. Fabregat-Santiago, J. Bisquert, Y. Sanehira, J. Nakazaki, H. Segawa, Enhanced carrier transport distance in colloidal PbS quantum-dot-based solar cells using ZnO nanowires. *J. Phys. Chem. C* **119**(49), 27265–27274 (2015). <https://doi.org/10.1021/acs.jpcc.5b09152>
24. S. Ozu, Y. Zhang, H. Yasuda, Y. Kitabatake, T. Toyoda et al., Improving photovoltaic performance of ZnO nanowires based colloidal quantum dot solar cells via SnO₂ passivation strategy. *Front. Energy Res.* **7**, 11 (2019). <https://doi.org/10.3389/fenrg.2019.00011>
25. P.H. Rekemeyer, S. Chang, C.H.M. Chuang, G.W. Hwang, M.G. Bawendi, S. Gradečak, Enhanced photocurrent in PbS quantum dot photovoltaics via ZnO nanowires and band alignment engineering. *Adv. Energy Mater.* **6**(24), 1600848 (2016). <https://doi.org/10.1002/aenm.201600848>
26. D. Bederak, D.M. Balazs, N.V. Sukharevska, A.G. Shulga, M. Abdu-Aguye, D.N. Dirin, M.V. Kovalenko, M.A. Loi, Comparing halide ligands in PbS colloidal quantum dots for field-effect transistors and solar cells. *ACS Appl. Nano Mater.* **1**(12), 6882–6889 (2018). <https://doi.org/10.1021/acsnano.8b01696>
27. J. Liu, G.H. Kim, Y. Xue, J.Y. Kim, J.B. Baek, M. Durstock, L. Dai, Graphene oxide nanoribbon as hole extraction layer to enhance efficiency and stability of polymer solar cells. *Adv. Mater.* **26**(5), 786–790 (2014). <https://doi.org/10.1002/adma.201302987>
28. D.-Y. Lee, S.-I. Na, S.-S. Kim, Graphene oxide/PEDOT:PSS composite hole transport layer for efficient and stable planar heterojunction perovskite solar cells. *Nanoscale* **8**, 1513–1522 (2016). <https://doi.org/10.1039/C5NR05271H>
29. M. Shanmugam, T. Bansal, C.A. Durcan, B. Yu, Multilayer graphene oxide/cadmium selenide quantum-dot-coated titanium dioxide heterojunction solar cell. *IEEE Electron Device Lett.* **33**(8), 1165–1167 (2012). <https://doi.org/10.1109/LED.2012.2201911>
30. L. Hu, D.B. Li, L. Gao, H. Tan, C. Chen et al., Graphene doping improved device performance of ZnMgO/PbS colloidal quantum dot photovoltaics. *Adv. Funct. Mater.* **26**(12), 1899–1907 (2016). <https://doi.org/10.1002/adfm.201505043>
31. J. Xu, H. Wang, Y. Wang, S. Yang, G. Ni, B. Zou, Efficiency enhancement for solution-processed PbS quantum dots solar cells by inserting graphene oxide as hole-transporting and interface modifying layer. *Org. Electron.* **58**, 270–275 (2018). <https://doi.org/10.1016/j.orgel.2018.04.021>
32. S. Stankovich, R.D. Piner, S.T. Nguyen, R.S. Ruoff, Synthesis and exfoliation of isocyanate-treated graphene oxide nanoplatelets. *Carbon* **44**(15), 3342–3347 (2006). <https://doi.org/10.1016/j.carbon.2006.06.004>
33. R.L.D. Whitby, A. Korobeinyk, V.M. Gun'ko, R. Busquets, A.B. Cundy et al., pH-driven physicochemical conformational changes of single-layer graphene oxide. *Chem. Commun.* **47**(34), 9645–9647 (2011). <https://doi.org/10.1039/C1CC13725E>
34. C.J. Shih, S. Lin, R. Sharma, M.S. Strano, D. Blankschtein, Understanding the pH-dependent behavior of graphene oxide aqueous solutions: a comparative experimental and molecular dynamics simulation study. *Langmuir* **28**(1), 235–241 (2012). <https://doi.org/10.1021/la203607w>
35. Y.L. Li, P.N. Yeh, S. Sharma, S.A. Chen, Promotion of performances of quantum dot solar cell and its tandem solar cell with low bandgap polymer (PTB7-Th): PC71BM by water vapor treatment on quantum dot layer on its surface. *J. Mater. Chem. A* **5**(40), 21528–21535 (2017). <https://doi.org/10.1039/C7TA04955B>
36. Y. Xia, S. Liu, K. Wang, X. Yang, L. Lian et al., Cation-exchange synthesis of highly monodisperse PbS quantum dots from ZnS nanorods for efficient infrared solar cells. *Adv. Funct. Mater.* **30**(4), 1907379 (2019). <https://doi.org/10.1002/adfm.201907379>
37. M. Li, B. Li, G. Cao, J. Tian, Monolithic MAPbI₃ films for high-efficiency solar cells via coordination and a heat assisted process. *J. Mater. Chem. A* **5**(40), 21313–21319 (2017). <https://doi.org/10.1039/C7TA06766F>
38. L. Gao, K. Zeng, J. Guo, C. Ge, J. Du et al., Passivated single-crystalline CH₃NH₃PbI₃ nanowire photodetector with high detectivity and polarization sensitivity. *Nano Lett.* **16**(12), 7446–7454 (2016). <https://doi.org/10.1021/acs.nanolett.6b03119>
39. Y. Cho, B. Hou, J. Lim, S. Lee, S. Pak et al., Balancing charge carrier transport in a quantum dot p-n junction toward hysteresis-free high-performance solar cells. *ACS Energy Lett.* **3**(4), 1036–1043 (2018). <https://doi.org/10.1021/acsenenergyl.8b00130>
40. J.A. Geurtz, Theory of space-charge-limited currents in thin semiconductor layers. *Phys. Status Solidi B* **15**(1), 107–118 (1966). <https://doi.org/10.1002/pssb.19660150108>
41. I. Moreels, G. Allan, B. De Geyter, L. Wirtz, C. Delerue, Z. Hens, Dielectric function of colloidal lead chalcogenide quantum dots obtained by a Kramers-Krönig analysis of the absorbance spectrum. *Phys. Rev. B* **81**(23), 235319 (2010). <https://doi.org/10.1103/PhysRevB.81.235319>
42. H. Li, G. Wu, W. Li, Y. Zhang, Z. Liu, D. Wang, S. Liu, Additive engineering to grow micron-sized grains for stable high efficiency perovskite solar cells. *Adv. Sci.* **6**(18), 1901241 (2019). <https://doi.org/10.1002/advs.201901241>
43. A.K. Rath, F. Pelayo Garcia de Arquer, A. Stavrinadis, T. Lasanta, M. Bernechea, S.L. Diedenhofen, G. Konstantatos, Remote trap passivation in colloidal quantum dot bulk nano-heterojunctions and its effect in solution-processed solar cells. *Adv. Mater.* **26**(27), 4741–4747 (2014). <https://doi.org/10.1002/adma.201400297>
44. G.W. Guglietta, B.T. Diroll, E.A. Gaulding, J.L. Fordham, S. Li, C.B. Murray, J.B. Baxter, Lifetime, mobility, and diffusion of photoexcited carriers in ligand-exchanged lead selenide nanocrystal films measured by time-resolved terahertz spectroscopy. *ACS Nano* **9**(2), 1820–1828 (2015). <https://doi.org/10.1021/nn506724h>



-
45. J.M. Luther, M. Law, Q. Song, C.L. Perkins, M.C. Beard, A.J. Nozik, Structural, optical, and electrical properties of self-assembled films of PbSe nanocrystals treated with 1,2-ethanedithiol. *ACS Nano* **2**(2), 271–280 (2008). <https://doi.org/10.1021/nn7003348>
46. C.H.M. Chuang, A. Maurano, R.E. Brandt, G.W. Hwang, J. Jean, T. Buonassisi, V. Bulović, M.G. Bawendi, Open-circuit voltage deficit, radiative sub-bandgap states, and prospects in quantum dot solar cells. *Nano Lett.* **15**(5), 3286–3294 (2015). <https://doi.org/10.1021/acs.nanolett.5b00513>